Optimization of particle image velocimeters. I. Double pulsed systems

1990 Meas. Sci. Technol. 1 1202

(http://iopscience.iop.org/0957-0233/1/11/013)

Meas. Sci. Technol. 1 (1990) 1202–1215. Printed in the UK

Optimization of particle image velocimeters. Part I: Double pulsed systems

Richard D Keane and Ronald J Adrian

Department of Theoretical and Applied Mechanics, University of Illinois at Urbana-Champaign, 104 South Wright Street, Urbana, IL 61801, USA

Received 13 February 1990, in final form 1 June 1990, accepted for publication 26 June 1990

Abstract. The spatial resolution, detection rate, accuracy and reliability of a particle image velocimeter depend critically upon the careful selection of a number of parameters of the PIV system and the fluid motion. An analytical model and a Monte Carlo computer simulation have been developed to analyse the effects of experimental parameters and to optimize the system parameters. A set of six non-dimensional parameters that are the most significant in optimizing PIV performance are identified. They are the data validation criterion, the particle image density, the relative in-plane image displacement, the relative out-of-plane displacement, a velocity gradient parameter and the ratio of the mean image diameter to the interrogation spot diamater.

These parameters are studied for the case of interrogation by autocorrelation analysis. By a single transformation, these results can be applied to interrogation by two-dimensional Fourier transform analysis of the Young's fringes.

It is shown that double pulsed systems operate best when the image density exceeds 10–20 and the maximum relative in-plane and out-of-plane displacements do not exceed 30%. Velocity gradients reduce the valid data rate, and they introduce a small statistical bias. Corrections for the statistical bias are developed, with recommendations for minimizing bias effects and loss of signal strength.

1. Introduction

Particle image velocimetry (PIV) is a quantitative method of measuring velocity fields instantaneously in experimental fluid mechanics (Simpkins and Dudderar 1978, Barker and Fourney 1977, Adrian 1986, Meynart 1983, Grousson and Mallick 1977, Dudderar *et al* 1988, Hesselink 1988, Lauterborn and Vogel 1984). In a double pulsed planar PIV system, two light pulses of intensity $I_{01}(\boldsymbol{x})$ and $I_{02}(\boldsymbol{x})$ separated by a time interval Δt, illuminate a light sheet of thickness Δz_0 (as shown in figure 1) to produce a double exposed single photographic frame having pairs of particle images from which simultaneous in-plane velocity measurements result.

The position in the image plane $\boldsymbol{X}=(X, Y)$ for erected images is related to the position in the fluid $\boldsymbol{x}=(x, y, z)$ by

$$\boldsymbol{X}=\frac{d_i}{d_0-z}(x\hat{\boldsymbol{x}}+y\hat{\boldsymbol{y}}). \tag{1}$$

Thus, the local in-plane image displacement between pulses, $d\boldsymbol{X}$, is related to the velocity $\boldsymbol{u}=(u, v, w)$ by

$$d\boldsymbol{X}=(dX, dY)=M(u\hat{\boldsymbol{x}}+v\hat{\boldsymbol{y}})\Delta t+M\frac{\boldsymbol{x}}{d_0-z}(w\Delta t). \tag{2}$$

In paraxial recording this reduces to

$$d\boldsymbol{X}=M(dx\hat{\boldsymbol{x}}+dy\hat{\boldsymbol{y}}) \qquad \text{where} \qquad |\boldsymbol{X}|/d_0 \ll 1. \tag{3}$$

The interrogation procedure for measuring the displacement, $d\boldsymbol{X}$, is carried out by illuminating a small interrogation spot, centred on $\boldsymbol{X}_I$ and with diameter d_I, with an interrogation beam of intensity $I_I(\boldsymbol{X})$. The displacement of particle image pairs, $\Delta\boldsymbol{X}(\boldsymbol{X}_I)$, is determined and scanning $\boldsymbol{X}_I$ over the entire photograph produces displacements over the entire image plane. The measured in-plane velocity is determined by

$$\boldsymbol{u}_m(\boldsymbol{x}_I)=\Delta\boldsymbol{X}(\boldsymbol{X}_I)/M\Delta t \tag{4}$$

where $\boldsymbol{x}_I$ is the location in the fluid corresponding to the interrogation spot location on the photograph $\boldsymbol{X}_I$.

The Young's fringe method and the direct imaging method are utilized to obtain the mean displacement of particle images for each interrogation spot. In the direct imaging method, the physical image plane is digitized and analysed completely within the computer. When the image density, N_I, defined to be the mean number of particles per interrogation spot, is too high to allow individual image pairs to be identified, a statistical method of analysis such as correlation is used (Adrian 1986). The

0957-0233/90/111202+14 $03.50

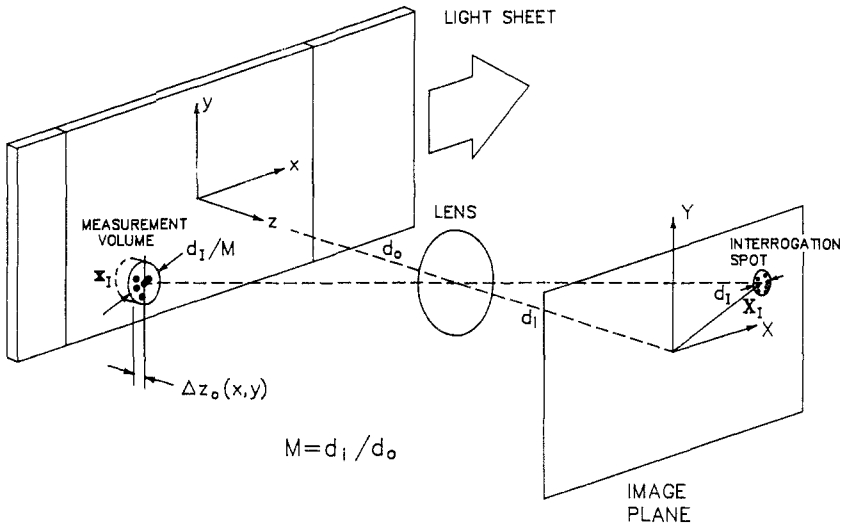

Figure 1. Light sheet and image recording system for planar pulsed laser velocimetry.

autocorrelation of particle image intensities over the interrogation spot is analysed to determine mean image displacements from peak values in the autocorrelation function.

In the Young's fringe method of interrogation, the image field of the interrogation spot is Fourier transformed by a lens so that each pair of particle images produces a system of interference fringes whose spacing is inversely proportional to the image spacing and whose orientation is perpendicular to the image displacement vector (Burch and Tokarski 1968, Meynart 1983). The displacement and orientation of the Young's fringe pattern are found by taking a two-dimensional (2-D) Fourier transform of the digitized Young's fringe data.

The full 2-D correlation and the full 2-D Fourier transform of Young's fringe methods each use all of the digitized data and concentrate the signal energy into peaks that are almost optimally narrow, so it is reasonable to expect that the results obtained from them constitute upper bounds on the performance of less complete methods of analysis, which involve multiple one-dimensional Fourier transforms of the digitized data and are reviewed elsewhere (cf Yao and Adrian 1984, for example). In general, all of these methods achieve enhanced computational rates by sacrificing some of the image information, either through using only a subset of the image data or through reducing the number of image data by averaging or spatial filtering. Likewise, photographic parameters and marker particle characteristics are not expected to affect the details of the interrogation method. Hence, conclusions derived from PIV performance based on full 2-D correlation or on full 2-D Fourier transformation of the fringes will be useful and relatively universal guidelines to the optimization of PIV performance when other types of analysis are used.

The performance of PIV is determined by the spatial resolution, the detection rate and the accuracy of the velocity measurements. The spatial resolution is defined by the size of the measurement volume relative to the length scales of the flow field. The detection rate is defined as the number of interrogation spots per unit area of image plane that produce velocity measurements which satisfy certain interrogation criteria. The accuracy of the velocity data is determined by the interrogation method, the optics and the nature of the velocity field. The accuracy of all detections that satisfy the interrogation criteria, whether they are valid or not, measures the ability of the interrogation criteria to produce valid measurements which agree with a known velocity field. These three parameters are affected by the experimental configuration, the interrogation procedure and its criteria and in turn depend upon: the mean concentration of seeding particles, C, the character of the flow field, $\boldsymbol{u}(\boldsymbol{x})$ as determined by the local velocity at the centre of the measurement volume and the velocity variations within the measurement volume, the thickness of the light sheet, Δz_0, the time interval between exposures, Δt, and the size, d_I, and shape of the interrogation spot. The foregoing variables depend upon the lens magnification, M, the wavelength of the pulsed light, λ, and the f-number of the camera lens, $f^\#$, which determine the particle image diameters, d_τ, from known particle diameters, d_p. To optimize the performance of PIV it is necessary to understand the influence of all of these parameters.

In the present paper, an analytical model is developed and used with a Monte Carlo simulation of a double pulsed planar PIV system to optimize the performance of PIV for a full 2-D interrogation by either spatial correlation or Young's fringes. Paraxial image recording is assumed for simplicity. The marker particles have a constant diameter so that the particle images have equal diameters. The recording film properties are linear and there is assumed to be no noise background in the image field and the N_I is sufficiently low to discount the probability of images overlapping. Locally linear, three-dimensional velocity fields are considered.

The experimental and interrogation parameters can be reduced to a smaller set of dimensionless parameters.

The particle image density, N_I, is defined for a circular interrogation spot to be

$$N_I = C \frac{\pi d_I^2}{4M^2} \Delta z_0. \tag{5}$$

The dimensionless mean displacement of particle images in an interrogation spot relative to the spot diameter is $|\Delta X|/d_I$. The appropriate dimensionless out-of-plane motion of the particles in the light sheet is $\Delta z/\Delta z_0$ where $\Delta z = w\Delta t$ is the out-of-plane displacement. The extent of image displacement variation within an interrogation spot caused by velocity gradients can be expressed in terms of d_τ and d_I. The optimal value and acceptable range for N_I, $|\Delta X|/d_I, w\Delta t/\Delta z_0$, velocity variations and a non-dimensional detectability criterion D_0, to be defined later, will be determined in terms of given experimental parameters.

The above non-dimensional parameters are important for both methods of interrogation whose similarity is demonstrated in the next section, while differences between the optimal parameters for each method are explained where appropriate.

2. Interrogation methods

2.1. Spatial correlation

When a photograph is interrogated by a light beam of intensity $I_I(X - X_I)$ centred at X_I, the transmitted light intensity immediately after the photograph is

$$I(X) = I_I(X - X_I)\tau(X) \tag{6}$$

where $\tau(X)$, the intensity transmissivity of the photograph is

$$\tau(X) = \sum_i [I_{01}(x_i)\tau_0(X - Mx_i(t)) + I_{02}(x_i)\tau_0(X - Mx_i(t + \Delta t))] \tag{7}$$

given the model assumptions stated above and where $x_i(t)$ is the location of the ith particle at time t. The value $\tau_0(X - Mx)$ represents the transmissivity of an individual particle image per unit of illuminating intensity in the light sheet and is the same for every particle.

The spatial autocorrelation of $I(X)$ with separation s is approximated by the following spatial average estimator over an interrogation spot

$$R(s) = \int I(X)I(X + s)\,dX. \tag{8}$$

Using notation of Adrian (1988a), it can be shown that the estimator consists of five components

$$R(s) = R_C(s) + R_P(s) + R_{D^+}(s) + R_{D^-}(s) + R_F(s) \tag{9}$$

Figure 2(*a*) illustrates the components of the correlation function for a single interrogation spot in which a velocity field across the spot is constant and it contains $N_I = 15$ randomly located particles. $I_I(X)$ is a constant intensity over the interrogation spot and the particle image transmissivity, τ_0 is modelled as a Gaussian function with diameter d_τ. The light sheets are identical with constant intensity $I_{01} = I_{02} = I_0$ inside the sheet and zero intensity outside. Then

$$\tau(X) = I_0 \sum_i [\tau_0(X - X_i(t)) + \tau_0(X - X_i(t + \Delta t))] \tag{10}$$

where i is summed over all particles within the sheet, and $X_i(t)$ is the location of the ith particle image at time t.

The mean image displacement across the interrogation spot is determined by locating the centroid of R_{D^+}

$$\bar{\mu}_{D^+} = \frac{\int sR_{D^+}(s)\,ds}{\int R_{D^+}(s)\,ds} \tag{11}$$

where $\bar{\mu}_{D^+}$ is an estimate of the mean translation ΔX that appears in equation (5).

The mean velocity is then estimated by $\bar{\mu}_{D^+}/M\Delta t$. With no *a priori* knowledge of $R_{D^+}(s)$, $\bar{\mu}_{D^+}$ can be estimated by locating s_{D^+}, the position of the peak value of $R_{D^+}(s)$, by a search over the s-plane, taking into account the self-correlation peak R_P at the origin. This assumes that the tallest peak is the R_{D^+} peak although the random noise peaks from $(R_C + R_F)$ can sometimes exceed the peak of R_{D^+}. The centroid of R_{D^+} is then approximated by integration over a region around the peak value s_{D^+}, the details of which will be discussed later in section 4, where algorithms are described.

2.2. Young's fringe method

The amplitude transmissivity of the image recorded on the film, $t(X)$, is related to the intensity transmissivity, $\tau(X)$, by

$$t(X) = \tau(X)^{1/2} e^{i\theta(X)} \tag{12}$$

where $\theta(X)$ is the phase of the amplitude transmissivity.

The scalar light field from the interrogation spot is given by

$$E(X) = I_I(X - X_I)^{1/2} t(X). \tag{13}$$

The Young's fringes are obtained by taking the Fourier transform of the scalar light field. The scalar field at x_f in the Young's fringe plane can then be written as

$$\hat{E}(x_f) = \int \exp\left(-\frac{2\pi i}{\lambda f} X \cdot x_f\right) E(X)\,dX \tag{14}$$

where f is the focal length of the Fourier transform lens and λ is the wavelength of the interrogation beam. The intensity of the fringe pattern is

$$I_f(x_f) = |\hat{E}(x_f)|^2 = \hat{E}(x_f)\hat{E}^*(x_f). \tag{15}$$

It can be digitized by an electronic camera and analysed by two-dimensional Fourier transformation, e.g.

$$G(s) = \frac{1}{4\pi^2} \int \exp\left(\frac{2\pi i}{\lambda f} s \cdot x_f\right) I_f(x_f)\,dx_f \tag{16}$$

where s is the variable in the numerically computed Fourier transform plane. By the convolution theorem, $G(s)$ is equal to the convolution of the Fourier

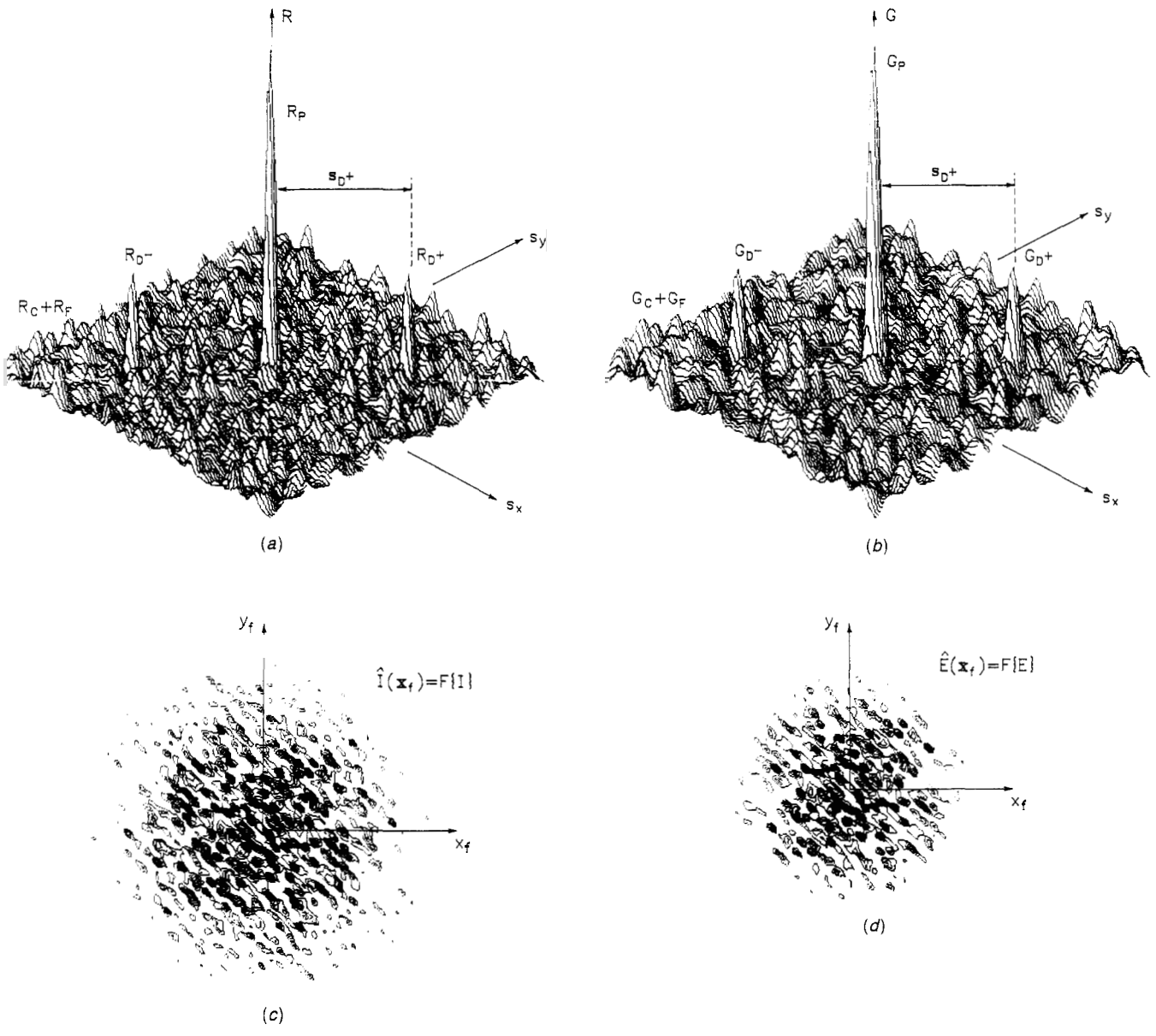

Figure 2. (*a*) Correlation function R for constant velocity within the measurement volume. $N_I = 15$ and mean image displacement, $\Delta \boldsymbol{X}/d_\tau = (0.25, 0.25)$. (*b*) Correlation function G for image transmissivity amplitude $E(\boldsymbol{X})$. (*c*) |FFT of particle image intensity $I(\boldsymbol{X})|^2$. (*d*) |FFT of particle image amplitude $E(\boldsymbol{X})|^2$.

transforms:

$$G(\boldsymbol{s}) = \frac{f^2\lambda^2}{4\pi^2}\int E(\boldsymbol{X})E^*(\boldsymbol{X}-\boldsymbol{s})\,\mathrm{d}\boldsymbol{X}. \tag{17}$$

This convolution is very similar to the direct imaging correlation function defined in equation (8), with the transmitted light amplitude, $E(\boldsymbol{X})$, replacing the transmitted light intensity, $I(\boldsymbol{X})$. While the direct imaging method uses the erected image, the Fourier transform of the Young's fringe pattern does not, having no effect on $G(\boldsymbol{s})$ due to its reflectional symmetry.

The Fourier transform of the Young's fringe pattern can be decomposed into five components in a manner similar to equation (9), namely

$$G(\boldsymbol{s}) = G_C(\boldsymbol{s}) + G_P(\boldsymbol{s}) + G_{D^+}(\boldsymbol{s}) + G_{D^-}(\boldsymbol{s}) + G_F(\boldsymbol{s}). \tag{18}$$

Once again, the mean image displacement across the interrogation spot is determined by locating the centroid of G_{D^+} in a manner similar to equation (11).

To illustrate the relationship between the two methods of calculating displacement, consider the example of figure 2 wherein the particle image transmissivities were modelled as Gaussian functions of constant diameter d_τ, in equation (24) and the interrogation intensity, $I_I(\boldsymbol{x})$, was constant over the interrogation spot. As no images overlap, the particle image amplitude transmissivities are additive, giving

$$t(\boldsymbol{X}) = \sum t_0(\boldsymbol{X}-\boldsymbol{X}_i) \tag{19}$$

where

$$t_0(\boldsymbol{X}-\boldsymbol{X}_i) = \sqrt{\tau_0(\boldsymbol{X}-\boldsymbol{X}_i)}\exp\left[i\theta(\boldsymbol{X}-\boldsymbol{X}_i)\right]. \tag{20}$$

As the diameter of t_0 is $\sqrt{2}d_\tau$, the diameter of G_{D^+} is wider than that of R_{D^+} by a factor of $\sqrt{2}$. However, the

location of the peak in $G_{D^+}(s)$ is identical to the location of R_{D^+}, in the mean (figure 2(*b*)). Figure 2(*d*) illustrates the Young's fringe pattern obtained for the parameters cited above, and figure 2(*b*) illustrates the full two-dimensional Fourier transform of the fringes.

3. Mean autocorrelation and mean Fourier transform of Young's fringes

3.1. General velocity fields

To determine the statistical properties of R, we consider an ensemble of photographs of identical velocity fields in which each realization contains different sets of randomly located particles. For a known velocity field, $\boldsymbol{u}(\boldsymbol{x})$, the conditional average $\langle R(\boldsymbol{s})|\boldsymbol{u}\rangle$ calculated over random particle locations measures the mean behaviour of R given the flow field, $\boldsymbol{u}$.

The conditional average of R is determined by conditionally averaging equation (9):

$$\langle R(\boldsymbol{s})|\boldsymbol{u}\rangle = \langle R_C(\boldsymbol{s})|\boldsymbol{u}\rangle + \langle R_P(\boldsymbol{s})|\boldsymbol{u}\rangle + \langle R_{D^+}(\boldsymbol{s})|\boldsymbol{u}\rangle + \langle R_{D^-}(\boldsymbol{s})|\boldsymbol{u}\rangle \tag{21}$$

where it can be shown that $\langle R_F(\boldsymbol{s})|\boldsymbol{u}\rangle = 0$.

To study the behaviour of $\langle R(\boldsymbol{s})|\boldsymbol{u}\rangle$ parametrically for a variety of velocity fields, specific models of the transmissivity functions and light intensities are employed. The intensities of the light pulses, I_{01} and I_{02}, are assumed to be top hat functions equal to I_0 within the light sheet and zero outside of it, while the interrogation beam intensity is modelled for computational simplicity as a Gaussian function centred at $\boldsymbol{X}_I$ with diameter d_I measured at the e^{-2} points. The particle images are assumed to be identical with the image transmissivity being a Gaussian curve centred at the image centre with diameter, d_τ where d_τ is, again an e^{-2} diameter. This is a good approximation to a real particle image less its diffraction rings which are normally weak. Thus we have

$$I_{01}(\boldsymbol{x}) = I_{02}(\boldsymbol{x}) = \begin{cases} I_0 & |z| < \Delta z_0/2 \\ 0 & \text{otherwise} \end{cases} \tag{22}$$

$$I_I(\boldsymbol{X} - \boldsymbol{X}_I) = I_{I0} \exp(-8|\boldsymbol{X} - \boldsymbol{X}_I|^2/d_I^2) \tag{23}$$

and

$$\tau_0(\boldsymbol{X}) = \frac{8\tau_{00}}{\pi d_\tau^2} \exp(-8|\boldsymbol{X}|^2/d_\tau^2). \tag{24}$$

Here, $\tau_{00} = \int \tau_0 \mathrm{d}\boldsymbol{X}$, is determined by the photographic process and the development process.

The components of equation (21) for a general displacement field $\Delta\boldsymbol{x}(\boldsymbol{x}, t)$ become

$$\langle R_C(\boldsymbol{s})\rangle = \frac{4}{\pi} I_0^2 I_{I0}^2 \tau_{00}^2 \frac{N_I^2}{d_I^2} \exp\left(-\frac{4|\boldsymbol{s}|^2}{d_I^2}\right) \tag{25}$$

$$\langle R_P(\boldsymbol{s})\rangle = \frac{2}{\pi} I_0^2 I_{I0}^2 \tau_{00}^2 \frac{N_I}{d_\tau^2} \exp\left[-\frac{4|\boldsymbol{s}|^2}{d_\tau^2}\left(1 + \frac{d_\tau^2}{d_I^2}\right)\right] \tag{26}$$

$$\langle R_{D^+}(\boldsymbol{s})|\boldsymbol{u}\rangle = C \int \mathrm{d}\boldsymbol{x} I_0(z) I_0(z + \Delta z) \times \int \mathrm{d}\boldsymbol{X} I_{I0}^2 \exp(-8|\boldsymbol{X}|^2/d_I^2) \exp(-8|\boldsymbol{X} + \boldsymbol{s}|^2/d_I^2) \times \left(\frac{8\tau_{00}}{\pi d_\tau^2}\right)^2 \exp(-8|\boldsymbol{X} - M\boldsymbol{x}|^2/d_\tau^2) \times \exp(-8|\boldsymbol{X} - M\boldsymbol{x} + \boldsymbol{s} - M\Delta\boldsymbol{x}|^2/d_\tau^2). \tag{27}$$

These results are valid for arbitrary $\boldsymbol{u}$ through the displacement $\Delta\boldsymbol{x}$. If the velocity field does not evolve significantly between pulses, the simple relationship is

$$\Delta\boldsymbol{x}(\boldsymbol{x}, t) = \boldsymbol{u}(\boldsymbol{x}, t)\Delta t. \tag{28}$$

Both $\langle R_C(\boldsymbol{s})|\boldsymbol{u}\rangle$ and $\langle R_P(\boldsymbol{s})|\boldsymbol{u}\rangle$ are independent of the velocity field in the interrogation volume. $\langle R_C(\boldsymbol{s})\rangle$, approximately the convolution of the mean interrogation intensity with itself, is a broad function of $\boldsymbol{s}$ with diameter $\sqrt{2}\,d_I$ and an amplitude proportional to N_I^2. $\langle R_P(\boldsymbol{s})\rangle$, the mean of the correlation of each particle image with itself, is a narrow function of $\boldsymbol{s}$ with diameter $\sim\sqrt{2}\,d_\tau$. Its amplitude is proportional to the number of image pairs present, N_I. $\langle R_{D^+}(\boldsymbol{s})|\boldsymbol{u}\rangle$, the 'displacement' component of the correlation, depends upon the velocity field in the interrogation volume and it can be determined analytically for special cases of $\boldsymbol{u}(\boldsymbol{x}, t)$.

The statistical properties of $G(\boldsymbol{s})$, the Fourier transform of the Young's fringes are determined similarly by taking the conditional average of each term in equation (18). To compare the behaviour of $\langle G(\boldsymbol{s})|\boldsymbol{u}\rangle$ with that of $\langle R(\boldsymbol{s})|\boldsymbol{u}\rangle$, the specific model above is used.

Assuming that the image intensity transmissivity is given in equation (24), equation (20) gives the image amplitude transmissivity as

$$t_0(\boldsymbol{X} - \boldsymbol{X}_I) = \frac{2\sqrt{2}\sqrt{\tau_{00}}}{\sqrt{\pi}\,d_\tau} \times \exp(-4|\boldsymbol{X} - \boldsymbol{X}_I|^2/d_\tau^2) \exp[\mathrm{i}\theta(\boldsymbol{X} - \boldsymbol{X}_I)]. \tag{29}$$

All image transmissivity phases are assumed to be equal to zero.

With the interrogation beam intensity, I_I, modelled as before in equation (23), equation (13) becomes

$$E_I(\boldsymbol{X} - \boldsymbol{X}_I) = \sqrt{I_{I0}} \exp(-4|\boldsymbol{X} - \boldsymbol{X}_I^2|/d_I^2) \tag{30}$$

Thus, the components of $\langle G(\boldsymbol{s})|\boldsymbol{u}\rangle$ are

$$\langle G_C(\boldsymbol{s})\rangle = \frac{f^2\lambda^2}{\pi^2} I_0^2 I_{I0} \tau_{00} N_I^2 \frac{d_\tau^2}{d_I^2} \exp\left(-\frac{2|\boldsymbol{s}|^2}{d_I^2}\right) \tag{31}$$

$$\langle G_P(\boldsymbol{s})\rangle = \frac{f^2\lambda^2}{4\pi^2} I_0^2 I_{I0} \tau_{00} N_I \exp\left[-\frac{2|\boldsymbol{s}|^2}{d_\tau^2}\left(1 + \frac{d_\tau^2}{d_I^2}\right)\right] \tag{32}$$

$$\langle G_{D^+}(\boldsymbol{s})|\boldsymbol{u}\rangle = \frac{f^2\lambda^2}{4\pi^2} C \int \mathrm{d}\boldsymbol{x} I_0(z) I_0(z + \Delta z) \times \int \mathrm{d}\boldsymbol{X} I_{I0} \exp(-4|\boldsymbol{X}|^2/d_I^2) \times \exp(-4|\boldsymbol{X} - \boldsymbol{s}|^2/d_I^2) \frac{8\tau_{00}}{\pi d_\tau^2} \exp(-4|\boldsymbol{X} - M\boldsymbol{x}|^2/d_\tau^2) \times \exp(-4|\boldsymbol{X} - M\boldsymbol{x} - M\Delta\boldsymbol{x} - \boldsymbol{s}|^2/d_\tau^2). \tag{33}$$

$G_C(s)$ is a broad Gaussian function of s with diameter $2d_I$ while $G_P(s)$ is a narrow function of s with diameter $\sim 2d_\tau$ when it is assumed $d_\tau \ll d_I$.

3.2. Weak velocity gradients

When the velocity field varies slowly within the interrogation spot, it can be approximated by a locally constant velocity field evaluated at the centre of the measurement volume.

$$\boldsymbol{u}(\boldsymbol{x}) = \boldsymbol{u}_I = \boldsymbol{u}(\boldsymbol{x}_I). \tag{34}$$

Criteria to determine the validity of this approximation will be developed in the next section on strongly varying velocity fields. The present constant velocity analysis contains most of the important phenomena that affect the autocorrelation so that flow non-uniformity can often be neglected with good accuracy.

Given a constant velocity, the equations for the mean background component R_C and the mean pedestal component R_P remain as in equations (25) and (26). The mean displacement component simplifies to

$$\langle R_{D^+}(\boldsymbol{s})|\boldsymbol{u}\rangle = \frac{1}{\pi} I_0^2 I_{I0}^2 \tau_{00}^2 \frac{N_I}{d_\tau^2} F_0(w_I \Delta t) F_I(\boldsymbol{s}) \times \exp(-4|\boldsymbol{s} - M\boldsymbol{u}_I \Delta t|^2/d_\tau^2) \tag{35}$$

where

$$F_0(\Delta z) \equiv \int dz I_{01}(z) I_{02}(z + \Delta z) \Big/ \int dz I_{01}(z) I_{02}(z) \tag{36}$$

$$F_I(\boldsymbol{s}) \equiv \int d\boldsymbol{X} I_I(\boldsymbol{X}) I_I(\boldsymbol{X} + \boldsymbol{s}) \Big/ \int d\boldsymbol{X} I_I^2(\boldsymbol{X}) \tag{37a}$$

$$= \exp(-4|\boldsymbol{s}|^2/d_I^2). \tag{37b}$$

Equations (36) and (37*a*) are identical to those in Adrian (1988a). Equation (37*b*) follows from the assumed Gaussian form for $I_I(\boldsymbol{x})$ in equation (23). If $I_{01}(z)$ were assumed to be a Gaussian function with an e^{-2} width, Δz_0, then F_0 would be a Gaussian function with width $\sqrt{2}\,\Delta z_0$. In the present case, where we take I_0 to be a top hat function of width Δz_0, F_0 is a triangle function whose base is $2\Delta z_0$ wide. F_I is the normalized correlation of the interrogation intensity across the interrogation spot while $F_0(\Delta z)$ is the normalized correlation of the intensities of the two light pulses in terms of the particle displacements, $\Delta z_I = w_I \Delta t$ in the out-of-plane direction.

If the interrogation volume contains a random number N of randomly located particles at the instant of the first exposure, the maximum possible number of pairs of images that could contribute to R_{D^+} would be N. However, particle motion between exposures causes certain particles to leave the interrogation volume, so that the maximum number of true image pairs is less than N, and the amplitude of R_{D^+} is thereby reduced. We call this the *loss of pairs effect*. It is a consequence of out-of-plane motion, represented by F_0, and in-plane motion, represented by F_I. If I_I, I_{01} and I_{02} were uniform within the interrogation volume and zero outside it, then $F_0(w_I \Delta t) F_I(M\boldsymbol{u}_I \Delta t) N_I$ would represent the mean number of particles whose second images remained in the interrogation volume to produce a pair of images, where N_I is the mean value of N.

The effect of loss of pairs is seen most clearly by evaluating the displacement autocorrelation at $\boldsymbol{s} = M\boldsymbol{u}_I \Delta t$, where $\boldsymbol{u}_I$ in this context is the vector formed by the two in-plane components of velocity. From equation (35) the maximum value of R_{D^+} occurs very near this location when the image diameter is small. The mean value is

$$\langle R_{D^+}|\boldsymbol{u}\rangle = I_0^2 I_{I0}^2 \tau_{00}^2 F_0(w_I \Delta t) F_I(M\boldsymbol{u}_I \Delta t) N_I / \pi d_\tau^2. \tag{38}$$

The strength of R_{D^+} is proportional to the mean number of displacement pairs times the square of the interrogation intensity for one image times the area of an image. The amplitude of R_{D^+} decreases in direct proportion to the number of displaced image pairs left in the interrogation volume. If I_I, I_{01} and I_{02} are not top-hat distributions, then $F_0 F_I N_I$ should be interpreted as the mean number of pairs weighted by the light intensity distribution.

Two important operating criteria are derived from the simple requirement that the loss of pairs effect should not be too large. Since F_0 decreases in proportion to the relative out-of-plane motion, this dimensionless parameter $w_I \Delta t / \Delta z_0$ must be limited to a maximum value. Likewise, since F_I decreases in proportion to $M|\boldsymbol{u}_I|\Delta t/d_I$, (cf equation (37*b*)), the maximum in-plane displacement must be limited to a small fraction of d_I. The values recommended previously in Adrian (1988a), $\max(w_I \Delta t/z_0) = 0.5$ and $\max(M|\boldsymbol{u}_I|\Delta t/d_I) = 0.5$, yield $\min(F_I) = e^{-1}$ and $\min(F_0) = 0.5$. Recently, more conservative values, $\max(w_I \Delta t/\Delta z_0) = 0.25$ and $\max(M|\boldsymbol{u}_I|\Delta t/d_I) = 0.25$, have been recommended on the basis of practical experience with PIV interrogation (Adrian (1988b)).

Ideally, the maximum of $\langle R_{D^+}|\boldsymbol{u}\rangle$ is located at $M\boldsymbol{u}_I \Delta t$, but according to equation (35) the maximum is pulled toward $\boldsymbol{s} = \boldsymbol{0}$ by the factor $F_I(\boldsymbol{s})$ and located at

$$\boldsymbol{s}_{D^+} = M\boldsymbol{u}_I \Delta t/(1 + d_\tau^2/d_I^2) \tag{39}$$

Hence, simple detection of the peak of R_{D^+} (or its centroid) leads to an error of order d_τ^2/d_I^2. In experiments where care has been taken to minimize the image diameter, the error is negligible. For example, if $d_\tau = 20\ \mu$m and $d_I = 1$ mm, the error is 0.04%, which is negligible compared with the 0.5–1% error typically achieved in PIV measurements (Landreth *et al* 1988). If d_τ/d_I is allowed to exceed 0.1, the error exceeds 1%, and explicit correction should be made, assuming that adequate information about d_τ is available experimentally.

The ratio of the amplitude of the displacement correlation to the amplitude of the self-correlation provides a useful dimensionless measure of the signal quality. It is

$$\langle R_{D^+}(\boldsymbol{s}_{D^+})|\boldsymbol{u}\rangle / R_P(\boldsymbol{0}) = \tfrac{1}{2} F_0(w_I \Delta t) \times \exp[-4|M\boldsymbol{u}_I \Delta t|^2/(d_I^2 + d_\tau^2)]. \tag{40}$$

The ratio approaches one-half as the displacement approaches zero because the signal energy is split equally between R_{D^+} and R_{D^-}. It is always less than or equal to

one-half by virtue of the pair loss effect. The visibility of the fringe system obtained by Fourier transforming the autocorrelation function is equal to this ratio.

The analysis of the mean Fourier transform of the Young's fringes proceeds similarly, so that equation (33) becomes

$$\langle G_{D^+}(\boldsymbol{s})|\boldsymbol{u}\rangle = \frac{f^2\lambda^2}{8\pi^2} I_0^2 I_{10}\tau_{00} N_I F_0(w_I\Delta t) H_I(\boldsymbol{s}) \times \exp(-2|\boldsymbol{s} + M\boldsymbol{u}_I\Delta t|^2/d_\tau^2) \quad (41)$$

where

$$H_I(\boldsymbol{s}) \equiv \int d\boldsymbol{X} I_I^{1/2}(\boldsymbol{X}) I_I^{1/2}(\boldsymbol{X}+\boldsymbol{s}) \Big/ \int d\boldsymbol{X} I_I(\boldsymbol{X}) \quad (42a)$$

$$= \exp(-2|\boldsymbol{s}|^2/d_I^2). \quad (42b)$$

The peak of $\langle G_{D^+}|\boldsymbol{u}\rangle$ lies at that same point given for the autocorrelation in equation (39), although the Gaussian diameters are all broadened by a factor of $\sqrt{2}$. H_I measures the loss of pairs effect caused by in-plane motion, in a similar manner to F_I.

The ratios of amplitudes of $\langle G_{D^+}(\boldsymbol{s})|\boldsymbol{u}\rangle$ and $\langle G_{D^-}(\boldsymbol{s})|\boldsymbol{u}\rangle$ to that of $G_P(\boldsymbol{s})$ are identical to those of R after allowing for peak broadening, namely

$$\langle G_{D^+}(\boldsymbol{s}_{D^+})|\boldsymbol{u}\rangle / G_P(\boldsymbol{0}) = \tfrac{1}{2} F_0(w_I\Delta t) \exp\left(\frac{-2|M\boldsymbol{u}_I\Delta t|^2}{d_I^2 + d_\tau^2}\right). \quad (43)$$

3.3. Strong velocity gradients

In many experimental applications the effects of pair loss due to translation are small. However, the interrogation spot diameter, d_I, and the light sheet thickness, Δz_0, are frequently not small enough to warrant neglect of the velocity variations in the interrogation volume due to strong gradients, as in turbulent flow. Gradients distribute the image displacements over finite regions in the correlation plane which affects measurement in two ways.

The first effect is to necessitate careful interpretation of the relationship between the location of the displacement correlation and the mean fluid motion. It has been shown (Adrian 1988a) that the centroid of the expected value of R_{D^+} corresponds to a volume averaged velocity

$$\bar{\mu}_{D^+} = \int \boldsymbol{s}\langle R_{D^+}|\boldsymbol{u}\rangle \, d\boldsymbol{s} \Big/ \int \langle R_{D^+}|\boldsymbol{u}\rangle \, d\boldsymbol{s} \quad (44a)$$

$$= \int W(\boldsymbol{x}, \boldsymbol{X}, \boldsymbol{u})\boldsymbol{u}(\boldsymbol{x}, t)\, d\boldsymbol{x} \Big/ \int W(\boldsymbol{x}, \boldsymbol{X}, \boldsymbol{u})\, d\boldsymbol{x} \quad (44b)$$

wherein the weight function is given by

$$W = I_{01}(\boldsymbol{x}) I_{02}(\boldsymbol{x} + \boldsymbol{u}\Delta t) I_I(M\boldsymbol{x} - \boldsymbol{X}_I) I_I(M\boldsymbol{x} + M\boldsymbol{u}\Delta t - \boldsymbol{X}_I) \quad (45)$$

(The centroid of $\langle R_{D^+}|\boldsymbol{u}\rangle$ is not necessarily equal to the conditional mean of the centroid defined in equation (11) by virtue of random fluctuations in $\int R_{D^+}\, d\boldsymbol{s}$. We shall, however ignore this difference on the grounds that fluctuations in the denominator of (11) are larger than fluctuations in the numerator). Since W decreases with increasing $|\boldsymbol{u}|$, the measurement is statistically biased toward the lower speed particles. This bias can be made negligible. Firstly, its magnitude is bounded by the total variation of the velocity within the interrogation volume, so it is small if the gradients are weak. Secondly, limiting the displacements to constrain the loss of pairs effect on the amplitude of R_{D^+}, as recommended in section 3.2, also limits the variation of W with $\boldsymbol{u}$. To a first approximation,

$$W \simeq I_{01}(\boldsymbol{x}) I_{02}(\boldsymbol{x}) I_I^2(M\boldsymbol{x} - \boldsymbol{X}_I) \quad (46)$$

and the weight function depends only upon the light intensity distribution in the intersection of the interrogation spot with the illuminating beams.

The second, often more important, effect is that gradients diminish the amplitude of the correlation peak and broaden its width. When the amplitude becomes too small, the peak of the correlation function may not be detectable, resulting in failed measurements for regions of high velocity gradient.

Equation (46) provides a useful working definition of the measurement volume of a PIV. We shall refer to it as the small displacement measurement volume. Its e^{-2} diameter in the X–Y plane is $d_I/\sqrt{2}$ if the interrogation spot is a Gaussian with e^{-2} diameter d_I. Its thickness in the z-direction is Δz_0 if the light sheet has a top-hat intensity profile.

The behaviour of $\langle R_{D^+}|\boldsymbol{u}\rangle$ is analysed by expanding the velocity field within the measurement volume in a Taylor series about $\boldsymbol{x}_I$ and truncating at the first-order linear term:

$$u_i(\boldsymbol{x}) = u_i(\boldsymbol{x}_I) + (\partial u_i/\partial x_j)_{x_I}(x_j - x_{Ij}). \quad (47)$$

The results depend in general upon the deformation tensor $d_{ij} = \partial u_i/\partial x_j$, but for simplicity we shall consider two special cases: simply shear and pure rotation.

In the case of simple shear with $\partial u/\partial y \neq 0$, v, w constant it can be shown by direct calculation that

$$\langle R_{D^+}(\boldsymbol{s})|\boldsymbol{u}\rangle = \frac{1}{\pi} I_0^2 I_{I0}^2 \tau_{00}^2 \frac{N_I}{d_\tau^2} F_0(w_I\Delta t) \times [1 + (M\Delta u\Delta t/d_\tau)^2]^{1/2} \times \exp(-4|M\boldsymbol{u}_I\Delta t|^2/d_I^2) \exp[-4(s_y - Mv_I\Delta t)^2/d_\tau^2] \times \exp\{-4[1 + (M\Delta u\Delta t/d_\tau)^2]^{-1} \times \{s_x - [Mu_I\Delta t - Mu_I\Delta t(M\Delta u\Delta t/d_I)]\}^2/d_\tau^2\}. \quad (48)$$

Here Δu is the maximum variation in $\boldsymbol{u}$ across d_I

$$\Delta u = \left(\frac{\partial u}{\partial y}\right)_{x_I} \frac{d_I}{2M}. \quad (49)$$

Furthermore it is assumed that $d_\tau \ll d_I$ and second order effects of velocity variation are ignored.

The amplitude of R_{D^+} is diminished by the factor $[1 + (M\Delta u\Delta t/d_\tau)^2]^{1/2}$ in the presence of this velocity variation, decreasing the likelihood of detecting the dis-

placement peak. In addition, the diameter of the peak is broadened by the same factor in the direction of shear. The peak of R_{D^+} and its centroid are both located at

$$s_{D^+} = \left[Mu_I \Delta t - Mv_I \Delta t \left(\frac{M \Delta u \Delta t}{d_I} \right), Mv_I \Delta t \right]. \quad (50)$$

The second case we consider is a local rotational motion about the z-axis at x_I defined by $(\partial u/\partial y)_{x_I} = -(\partial y/\partial x)_{x_I}$ and all other components of the deformation tensor are equal to zero. We obtain

$$\langle R_{D^+}(s)|u\rangle = \frac{1}{\pi} I_0^2 I_{10}^2 \tau_{00}^2 \frac{N_I}{d_\tau^2} F_0(w_I \Delta t) \times [1 + (M \Delta u \Delta t/d_\tau)^2]^{-1} \exp(-4|Mu_I \Delta t|^2/d_I^2) \times \exp[-4(1 + (M \Delta u \Delta t/d_\tau)^2)^{-1} \times \{[s_x - (Mu_I \Delta t - Mv_I \Delta t(M \Delta u \Delta t/d_I))]^2 + [s_y - (Mv_I \Delta t - Mu_I \Delta t(M \Delta v \Delta t/d_I))]^2\}/d_\tau^2]. \quad (51)$$

The amplitude of R_{D^+} has been reduced by the factor $(1 + (M \Delta u \Delta t/d_\tau)^2)$ due to velocity variations in the u- and v-components of velocity and the Gaussian peak is broadened in each direction by the same factor as before. The peak and the centroid are now located at

$$s_{D^+} = \bar{\mu}_{D^+} = ((Mu_I \Delta t - Mv_I \Delta t(M \Delta u \Delta t/d_I)), (Mv_I \Delta t - Mu_I \Delta t(M \Delta v \Delta t/d_I))) \quad (52)$$

where $\Delta v = -\Delta u$ for a local rotation in the velocity field.

In each case above, the peak and the centroid of the mean of R_{D^+} are statistically biased towards velocities lower than u_I. We call this *gradient bias*. It occurs because the correlation is biased against the faster moving particle within the measurement volume. The extent of this gradient bias cannot exceed the maximum variation of velocity within the measurement volume and is determined by the dimensionless parameter $(M \Delta u \Delta t/d_I, M \Delta v \Delta t/d_I)$.

A second type of bias occurs because the peak amplitude of R_{D^+} is diminished, in the presence of a velocity gradient, by a factor which depends upon $M \Delta u \Delta t/d_\tau$. This consequence of the variation of particle image displacements from randomly located particles in the velocity field within the interrogation volume, lowers the probability of detecting the correlation peak among the noise peaks. We call this *detection bias*. When $M|\Delta u|\Delta t = d_\tau$ the reduction factors in equations (48) and (51) are $\sqrt{2}$ and 2 respectively, illustrating the need to minimize the variation in velocity within an interrogation volume by a judicious selection of Δt. In addition to biasing the estimate of the mean, the broadening of the displacement component, R_{D^+}, leads to increased uncertainty in estimating velocity from individual realizations.

In analysing the mean Fourier transform of the Young's fringes, $\langle G_{D^+}(s)|u\rangle$ the peak location s_{D^+}, and the extent of gradient bias are not affected by peak broadening factors and are identical to those in $\langle R_{D^+}(s)|u\rangle$. However, peak broadening and peak splintering increase the likelihood of detection bias in this method of analysis.

The close similarity between the spatial correlation and the 2-D Fourier transform of the Young's fringes is evident and the results for one form of analysis can be transferred directly into results for the other form. Consequently, the following sections will consider only the autocorrelation method, that being the most simply understood approach.

4. Autocorrelation fluctuations and performance

4.1. Validation

Interrogation performance is gauged in terms of the *spatial resolution*, the *data yield*, the *valid data yield*, and the *accuracy* of the measurements of data that are deemed to be valid. The data yield, or *detection* probability, is the probability that a single interrogation spot produces a velocity measurement that is acceptable according to certain validation criteria. The valid data yield, or valid detection probability, is the probability that a measurement judged to be valid is actually valid. All aspects of the performance are affected by random fluctuations of the autocorrelation function, and these in turn, are affected by the dimensionless parameters presented in the introduction, and by the specific details of the interrogation procedure.

The interrogation procedure locates the highest peak in $R(s)$, excluding the self-correlation peak R_P, and assumes that this peak corresponds to R_{D^+}. However, there is a non-negligible probability that the tallest peak is a noise peak, if the peak of the displacement correlation is comparable to the noise correlation level. To discriminate against this possibility, the tallest peak is required to be significantly stronger than the second tallest peak. This detectability criterion eliminates interrogations in which the displacement correlation is barely distinguishable from the noise, but it is not guaranteed to eliminate interrogations in which there is a very strong noise correlation peak.

The detectability is defined to be the ratio of the first tallest peak to the second tallest peak, located at s_1 and s_2, respectively (Adrian 1985):

$$D(X_I) = R(s_1)/R(s_2). \quad (53)$$

Because of the symmetry of $R(s)$, only one half of the plane needs to be searched. To validate the assumption that the tallest peak does indeed correspond to the displacement peak R_{D^+}, the detectability is compared to a threshold level D_0 which is a preset constant. The interrogation is accepted if $D \geqslant D_0$; the interrogation is rejected if $D < D_0$, i.e. if the correlation peak fails to exceed a certain signal-to-noise ratio.

The location s_1 estimates the mean displacement, namely $s_1 = \Delta X_I$. Then, the centroid of the correlation peak can be calculated by defining a small area A_1 around the peak, and integrating according to

$$\bar{\mu}_1 = \int_{A_1} sR \, ds \Big/ \int_{A_1} R \, ds. \quad (54)$$

The centroidal calculation offers accuracy greater than the resolution of the computational grid used in the s-plane. Since the grid spacing is defined by the pixel spacing of the device used to record the interrogation spot image field, this implies the possibility of locating the particle displacement to within an accuracy of a fraction of a pixel. The area A_1 should be defined in such a way that it contains only the displacement correlation peak, R_{D^+} and A_1 is defined here to be the area around s_1 in which $R(s)$ is greater than 1% of $R(s_1)$. Since R is the sum of R_{D^+}, R_C, and the random fluctuations R_F, the centroidal estimate is always contaminated, and it randomly fluctuates around a mean value that approximates to the mean displacement. The centroidal location becomes less accurate as velocity gradients broaden R_{D^+} and diminish its peak value, as discussed in section 3.

Invalid data are allowed by this criterion when the correlation of randomly located particle images, given by $R_C(s) + R_F(s)$, has a maximum larger than $R_{D^+}(s)$. The probability of such invalid data decreases as the detectability criterion, D_0, increases, as, however, does the probability of a successful interrogation. In order to determine an optimum value for D_0, which minimizes the occurrence of invalid data while maintaining a satisfactory probability of successful interrogations, a range of values for D_0 has been considered.

4.2. Monte Carlo simulation

The analysis of the mean correlation function, offers some insights into the performance of this interrogation procedure, but it cannot directly address questions concerning the probabilities of measurement and validation. Hence, a numerical simulation of the PIV image field and interrogation analysis has been constructed so that statistics of the detection probabilities can be found by Monte Carlo simulation.

An ensemble of 1200 realizations is generated for each velocity field in which particles are scattered randomly with an average N_I, governed by Poisson statistics. The seeded volume is sufficiently large to ensure no loss of particle images by restrictive boundaries from each interrogation volume. Both light sheet pulses have intensity as in equation (22) and the interrogation intensity, I_I is also constant across the square interrogation spots following experimental procedure unlike the analytical model in section 3, where I_I was defined as a Gaussian curve. The image transmissivity of the monodisperse particles image is given above in equation (24). The recording film properties are linear, the images interfere incoherently, i.e. N_I is sufficiently low to avoid image overlap and there is no background light noise level in the recording. Velocity gradients are assumed to be linear across the interrogation spot centred at x_I, as in equation (47).

Figure 3 shows a simulated region of the interrogation plane in which a constant in-plane velocity causes the image displacement, $\Delta X/d_I = (0.25, 0.25)$. Although $N_I = 15$, random fluctuations for individual interrogation spots are obvious.

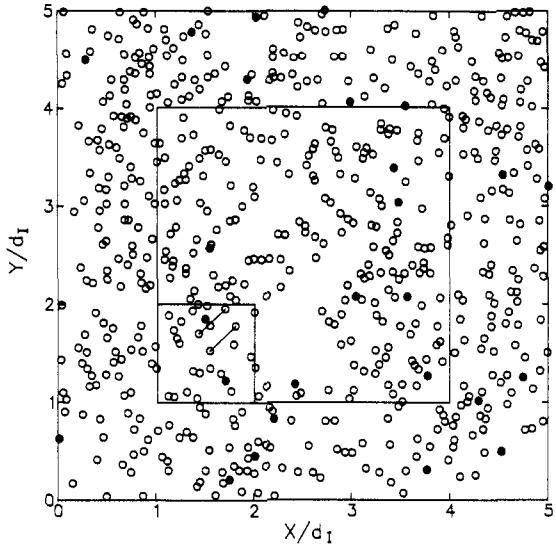

Figure 3. Simulated region of the interrogation plane. The velocity is constant within the measurement volume, $N_I = 15$ and the mean image displacement, $\Delta X/d_I = (0.25, 0.25)$. The smaller square denotes an interrogation spot.

The autocorrelation is computed using 2-D fast Fourier transforms of $I(X)$ digitized on a 256 × 256 array from each interrogation spot. Without padding the region around each spot with zeroes, the intensity I is effectively periodically extended, and a convolution of the periodic extension results. Figure 4 illustrates the mean correlation for 1200 realizations in which no zero padding of the intensity array was performed, resulting in a constant value for $\langle R_C(s) \rangle$ when I_{I0}, I_{01} and I_{02} were constant intensities. Zero padding of the intensity array could be achieved by embedding the 128 × 128 intensity array within a 256 × 256 array containing zeroes otherwise. As I would no longer be periodically extended, this would

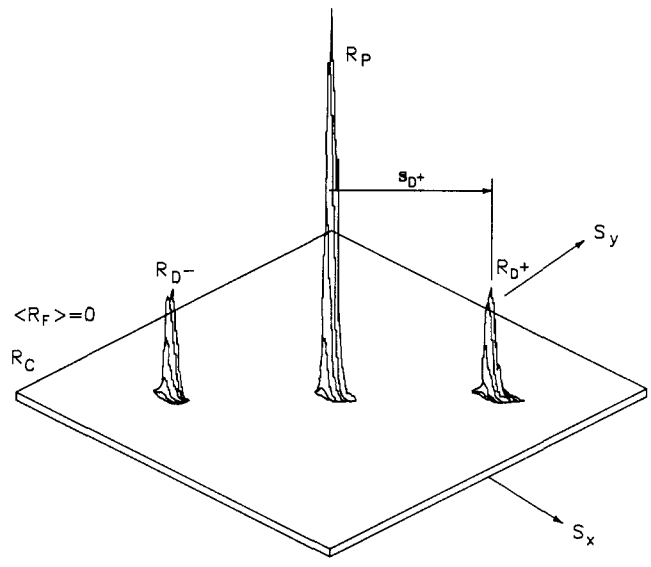

Figure 4. Expected value of correlation function R for constant velocity within the measurement volume. (Conditions as in figure 2.)

result in fewer noise peaks and a pyramidal form of $\langle R_C(s)\rangle$, thus improving the signal-to-noise ratio. However, as the spatial resolution is reduced and the valid detection probability is not significantly improved for the optimum parameters considered below, the use of no padding improves spatial resolution. The maximum image displacement is limited to $|\Delta X|/d_I \leqslant 0.5$ since it will be shown that larger displacements are undesirable. After determining D and u_m, a comparison is made between u_m and u_I to ascertain whether the measurement is valid or invalid, yielding both the detection probability and valid detection probability.

4.3. Performance: weak velocity gradients

The effect of variation of N_I is illustrated in figure 5 for a range of image displacements, $|\Delta X|/d_I$ using a detectability criterion of $D_0 = 1.5$ and constant in-plane velocities. Increasing N_I generally increases the detection probability and the valid detection probability because, from equation (35), the amplitude of R_{D+} is proportional to N_I. The minimum detection probability occurs when $N_I \approx 2$–3 because this low density does not give enough pairs to unambiguously define the correct pairing of images nor satisfy the detectability criterion, $D_0 = 1.5$. For lower values of N_I, the correct pairing of images does occur, but the total detection probability is low. This is the operating range studied by Landreth *et al* (1988). The estimate of $N_I \geqslant 4$ given by Lourenco and Krothapalli (1987) applies to a multiple pulsed PIV system and lies significantly below the optimal range for a double pulsed system. Recent analysis of multiple systems shows it is applicable when five or more pulses are employed.

As $|\Delta X|/d_I$ increases, fewer particle pairs remain in the interrogation spot as the first or second images move out of the spot. Because I_I is constant in the interrogation spot and zero elsewhere, F_I as defined in equation (37a) measures the ratio of the area that is common to both shifted and unshifted images to the total spot area. Thus, $N_I F_I$ is the mean number of image pairs in this region and is the effective number of image pairs in the spot.

To achieve a valid detection probability of at least 90%, the image density, N_I must be greater than 15 with $|\Delta X|/d_I < 0.3$. The valid detection rate is a decreasing function of relative displacement which declines sharply when $|\Delta X|/d_I$ exceeds 20–30% (figure 6). To achieve a high detection rate, the maximum value for $|\Delta X|/d_I$ is suggested to be 0.25. The choice of the time interval between light pulses, Δt, must then satisfy (cf Adrian 1988b).

$$\Delta t < 0.25 d_I / M \text{ Max } |u|. \tag{55}$$

The detectability threshold, D_0, is designed to minimize the false detection probability while ensuring an acceptable detection rate. There is an abrupt decrease in both the detection probability and the valid detection probability when $D_0 > 1.3$–1.5 for a wide range of N_I when a relative image displacement is $|\Delta X|/d_I = 0.30$ (figure 7). Relatively few peaks in R are stronger than $1.5\, R(s_2)$. Thus, a reasonable value for D_0 is in the range 1.2–1.5.

In the limit of small N_I, the probability of detection is equal to the probability of finding precisely one pair of images belonging to the same particle within the interrogation spot. This probability is given by the prob-

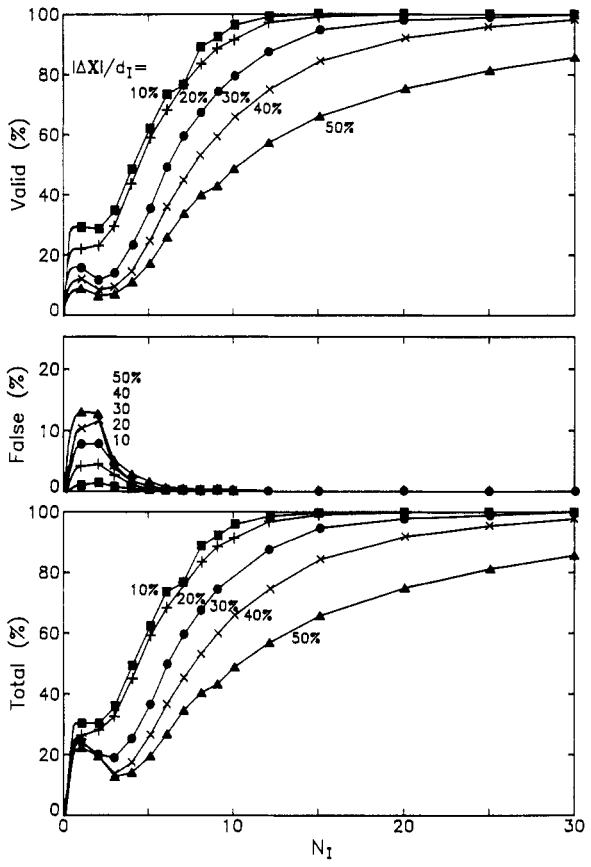

Figure 5. Total, false and valid detection probabilities as a function of relative image displacement $|\Delta X|/d_I$ and image density, N_I for $D_0 = 1.5$. The velocity within the interrogation spot is constant.

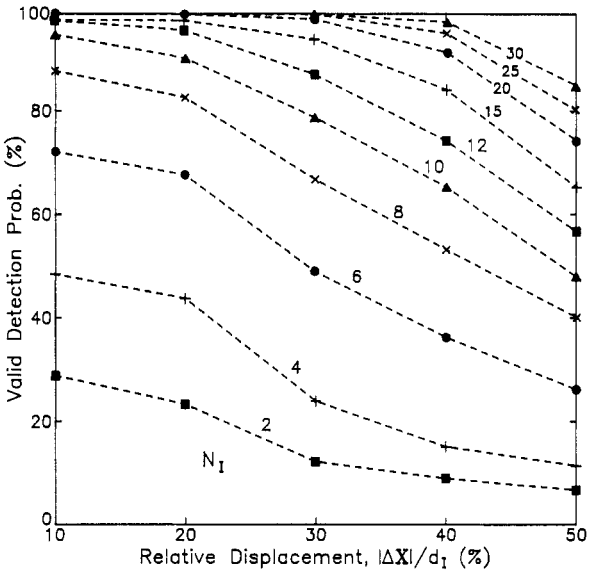

Figure 6. Valid detection probability versus relative image displacement $|\Delta X|/d_I$ for $D_0 = 1.5$ and variable particle image density, N_I.

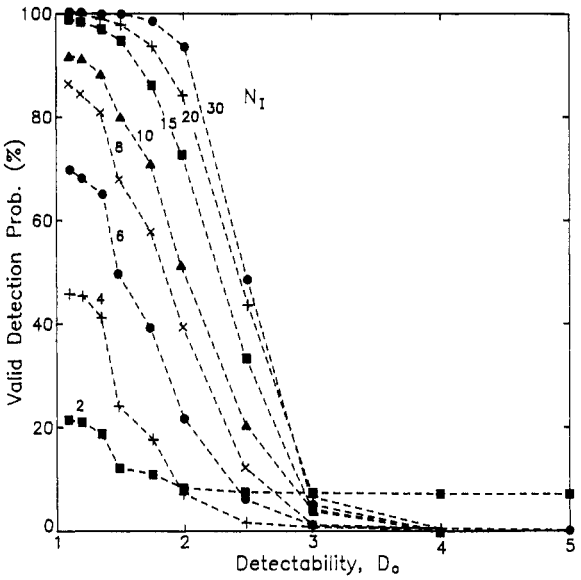

Figure 7. Valid detection probability as a function of detectability for variable particle image density N_I and $|\Delta \boldsymbol{X}|/d_I = 0.3$.

ability of finding one particle in that portion of the interrogation volume from which the particle could be displaced and still remain within the interrogation volume at the time of the second exposure. The average number of particles within this region is $N_I F_0 F_I$, and therefore from the Poisson distribution it follows that

$$\text{Prob \{exactly one pair of images\}} = N_I F_0 F_I \exp(-N_I F_0 F_I) \exp[-2N_I F_0(1-F_I)]. \quad (56)$$

This result shows that the effects of in-plane displacement, out-of-plane displacement and particle concentration can be correlated in terms of the single parameter $N_I F_0 F_I$ when the image density is small. Figure 8 confirms this correlation, and shows that equation (56) is valid for $N_I F_I$ less than about 0.3. These results are independent of D_0 due to the lack of noise peaks in $R(s)$. In low image density cases, the correlation procedure can be replaced by simpler methods such as orthogonal image compression (Yao and Adrian 1984), and the detection probability depends principally upon the probability of finding a true pair of images.

When the velocity includes a component perpendicular to the light sheet, the number of image pairs per interrogation spot is reduced, decreasing the peak amplitude of R_{D+} and increasing the contribution of $R_C + R_F$. Thus the valid detection probability decreases as the relative out-of-plane motion, $w\Delta t/\Delta z_0$ increases (figure 9). In the extreme case, where $w\Delta t/\Delta z_0 \geqslant 1$, the detection rate becomes zero, as no image pairs remain in the interrogation spot.

The detection probability for various values of N_I can be correlated in terms of $N_I F_0(\Delta z)$, which represents the mean number of particles that reside in the light sheet for both light pulses. Figure 10 correlates this probability

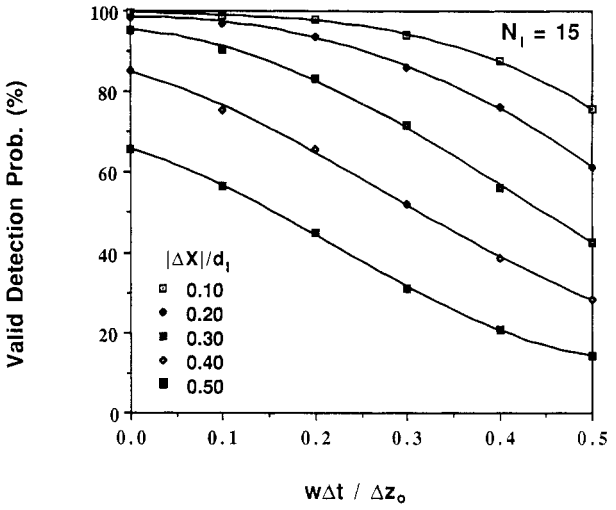

Figure 9. Valid detection probability as a function of the relative out-of-plane motion for $N_I = 15$ and $D_0 = 1.5$.

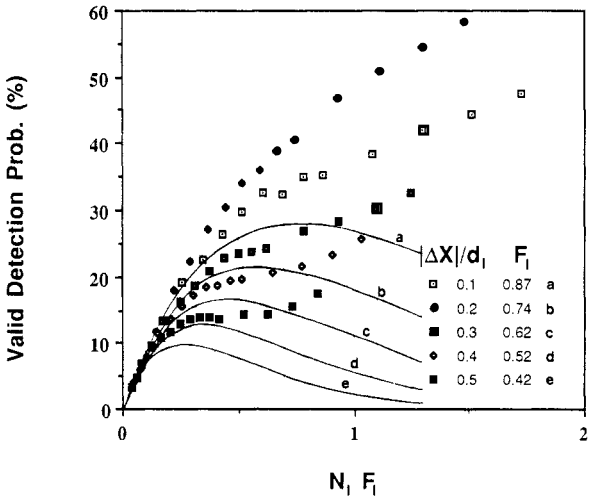

Figure 8. Valid detection probability for low image density; N_I in terms of the effective image density, $N_I F_I$, for detectability $D_0 = 1.5$. Full curves illustrate equation (56) with $F_0 = 1$ and F_I as tabulated.

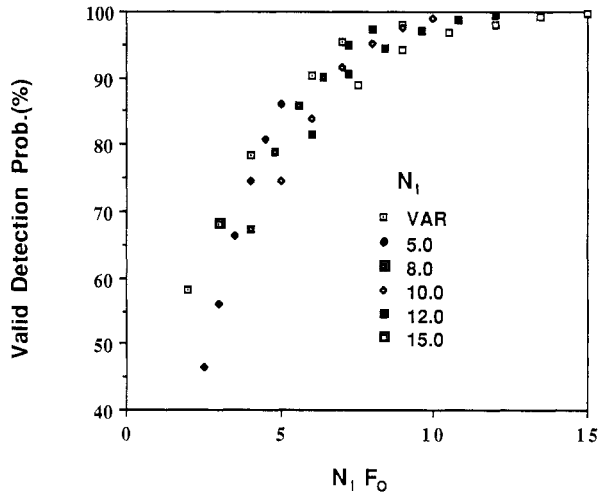

Figure 10. Correlation of the valid detection probability for out-of-plane displacements in terms of the effective image density, $N_I F_0$. Detectability $D_0 = 1.0$ and $|\Delta \boldsymbol{X}|/d_I = 0.2$.

with $N_I F_0$ for a range of N_I using $D_0 = 1.0$ and $|\Delta X|/d_I = 0.2$. Both figures 9 and 10 illustrate the need to select Δz_0 to minimize loss of detection rate without losing spatial resolution in the out-of-plane direction.

4.4. Performance: strong velocity gradients

As outlined in section 3, the effects of velocity gradients are to diminish the mean correlation peak while broadening its diameter, and to statistically bias the centroid of $\langle R_{D^+} | \boldsymbol{u} \rangle$ against high velocities. Figure 11 shows the correlation function of a single interrogation spot for conditions identical to those in figure 2, except that a simple shear, $\partial u/\partial y = 0.24 u_I/d_I$ has been added to the uniform translation. The decreased amplitude of R_{D^+} is apparent.

Figure 12 shows the detection probability as a function of the dimensionless velocity variation $M\Delta u\Delta t/d_\tau$ for various displacements $|\Delta X|/d_I$. The parameter $M\Delta u\Delta t/d_\tau$ is suggested by the theory for $\langle R_{D^+} | \boldsymbol{u} \rangle$ in which the amplitude is proportional to $[1 + (M\Delta u\Delta t/d_\tau)^2]^{-1/2}$. The detection probability is proportional to this amplitude with only a weak dependence upon $|\Delta X|/d_I$. Figure 12 indicates that high detection probabilities can be achieved if the velocity variation is such that $M\Delta u\Delta t/d_\tau < 1$, and $|\Delta X|/d_I < 0.25$, as indicated by the shaded area. The worst-case detection probability for operation within this area is 92%, and over much of the region the detection probability exceeds 98%. These values are consistent with experience derived from interrogation of experimental PIV photographs of turbulent flows (Reuss *et al* 1989, Landreth and Adrian 1989).

The constraints $M\Delta u\Delta t/d_\tau < 1$ and $|\Delta X|/d_I < 0.25$ imply that

$$\Delta u/u_I < 4d_\tau/d_I \tag{57}$$

which can be used to estimate the maximum velocity

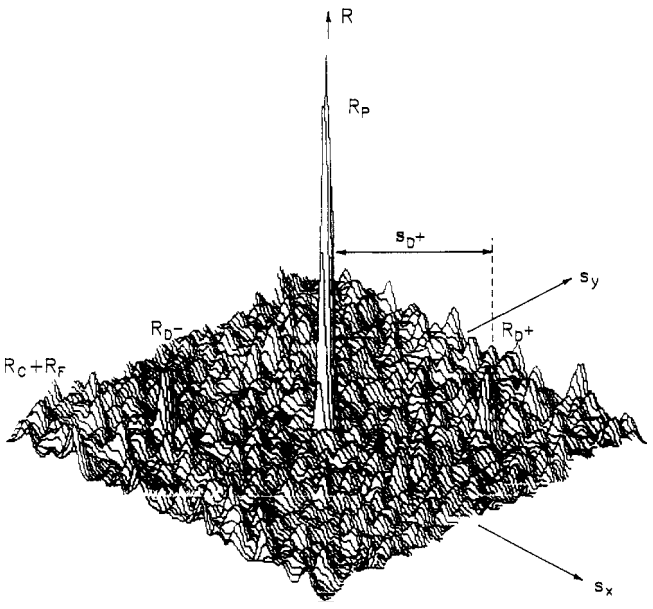

Figure 11. Correlation function R for a plane shearing velocity within the measurement volume. $N_I = 15$, $\Delta X/d_I = (0.25, 0.25)$, $(\partial u/\partial y)_x = 0.24 Mu_I/d_I$.

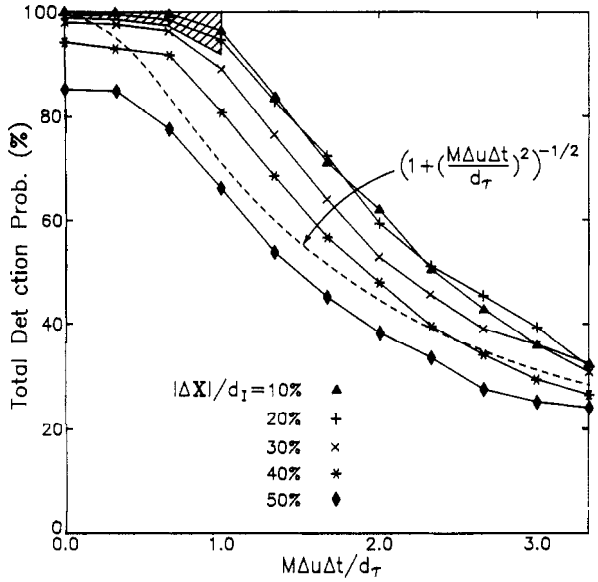

Figure 12. Total detection probability for a simple shear in terms of the relative image displacement variation, $M\Delta u\Delta t/d_\tau$, for variable image displacements, $|\Delta X|/d_I$, $N_I = 15$, $D_0 = 1.2$. -----, amplitude of $\langle R_{D^+} | \boldsymbol{u} \rangle$ from theory.

difference that can be comfortably treated by the correlation technique for a given interrogation spot diameter, or to define the diameter needed for a given maximum velocity variation. For example, if the total velocity variation across d_I is 40% ($\Delta u/u_I = 0.2$), and if the image diameter is 25 μm then the maximum interrogation spot size should be less than 0.5 mm. The requirement that N_I should exceed 15–20 places a lower bound on the size of the interrogation spot. Hence, velocity gradients ultimately place a fundamental limit on the measurements that can be made with double pulsed autocorrelation PIV. While other techniques such as multiple pulse recording or individual particle tracking may (or may not) offer some alleviation of these limits, it is clear that the smallest scales of motion that can be measured will also ultimately be limited by the diameter of the images. Thus, an inequality like equation (57) is expected to pertain to any type of PIV system, with the constant depending upon the system operation.

Velocity variation affects the accuracy of valid data measurements by statistically biasing measurements based on the centroid $R_{D^+}(s)$. For the simple shear velocity field, figures 13 and 14 relate the relative bias in the velocity component, u, to the variation of u. In figure 13, the bias is measured in terms of $M\Delta u\Delta t/d_I$ for a range of mean image displacements with $N_I = 15$ and $D_0 = 1.2$. The relative bias is independent of the mean image displacement, $|\Delta X|/d_I$, and varies linearly with $M\Delta u\Delta t/d_I$, in agreement with equation (50), which is based on analytical models with parameters similar to the parameters of the simulation.

The only way to reduce this bias is to reduce the time interval between pulses, but these measures also decrease the accuracy as $|\Delta X|$ decreases. In principle, the bias can be eliminated by using measurements of the velocity field to estimate gradients and then using a simple formula

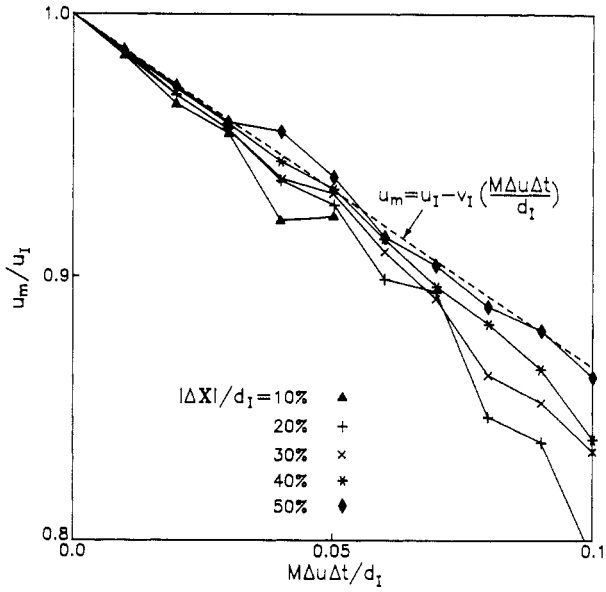

Figure 13. Relative measured mean velocity for a plane shearing velocity in terms of $M\Delta u\Delta t/d_I$. Conditions as in figure 12.

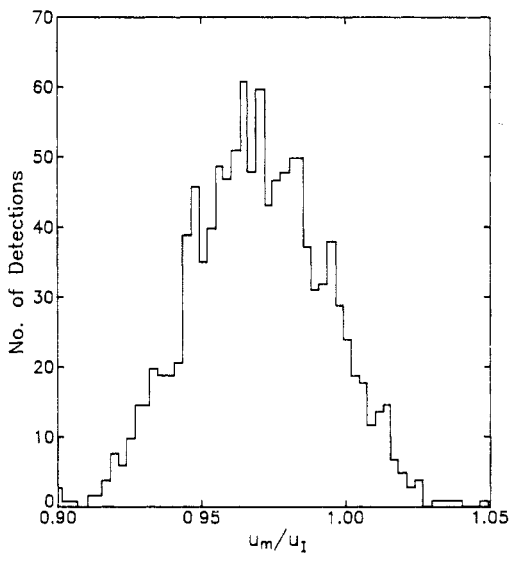

Figure 14. Variation in measured velocity for 1200 realizations where $N_I = 15$, $|\Delta \boldsymbol{X}|/d_I = 0.30$, $M\Delta u\Delta t/d_I = 0.02$ for detectability $D_0 = 1.2$.

like that in figure 13 to correct the measurements. Further work is needed to develop the equation for arbitrary gradients.

Finally, velocity variation causes random errors in valid measurements because the random particle locations within the varying velocity field cause R_{D+} to spread out over a discrete range of displacements which vary for each realization. A typical distribution of sample displacements from 1200 realizations is illustrated in figure 14 with $N_I = 15$, $D_0 = 1.2$, $|\Delta \boldsymbol{X}|/d_I = 0.3$. The mean and standard deviation of the distribution are $\langle u_m \rangle/u_I = 0.97$ and $\sigma_{u_m}/u_I = 0.024$. The 2.4% standard deviation compares with results by Landreth *et al* (1988). Figure 15 relates the rms of the random variation in u_m to the

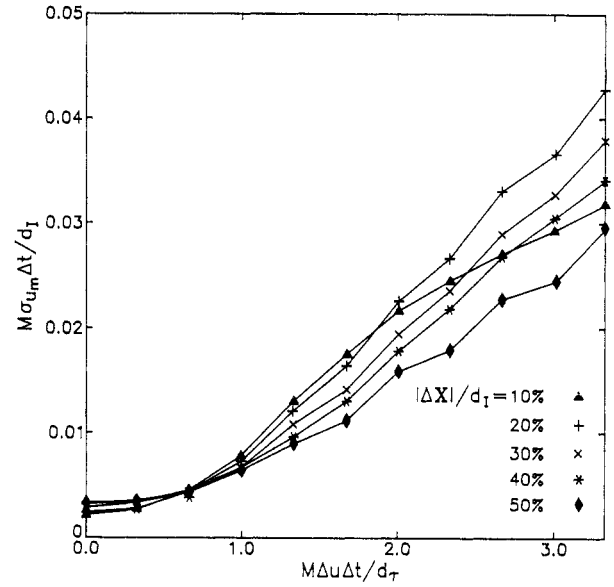

Figure 15. Variation in measured velocity in terms of the relative image displacement variation $M\Delta u\Delta t/d_\tau$ for variable image displacements $|\Delta \boldsymbol{X}|/d_I$, $N_I = 15$, $D_0 = 1.2$.

velocity variation due to gradients for $N_I = 15$ and $D_0 = 1.2$. To restrict the variation in u_m about its mean, which is already biased (equation (50)), the previous criterion for acceptable detection probability applies, ensuring $M\Delta u\Delta t/d_\tau \leqslant 1$. This produces an RMS variation in image displacement less than 0.8% of the spot size, d_I. The selection of Δt ensures an acceptable detection probability, degree of bias and variation in individual measured velocities about the measured mean.

5. Summary and conclusions

The two-pulse PIV method has been studied to optimize its performance for a range of velocity fields. Analyses by full 2-D spatial correlation of direct images and by 2-D Fourier transform of Young's fringes are shown to be equivalent with minor differences when analytical models based on experimental results are used for each approach. Theoretical analyses of both methods and a Monte Carlo simulation of the correlation method reveal the critical parameters of the mean autocorrelation and its fluctuations. The important dimensionless parameters, have been defined and investigated in the Monte Carlo simulation to determine their effect upon the performance of PIV. They are

$$N_I,\ D_0,\ |\Delta \boldsymbol{X}|/d_I,\ |\Delta \boldsymbol{u}|/|\boldsymbol{u}_I|,\ M|\Delta \boldsymbol{u}|\Delta t/d_\tau,\ d_\tau/d_I \text{ and } w\Delta t/\Delta z_0.$$

To optimize this performance, the following broad criteria are recommended; (*a*) $N_I \geqslant 15$, (*b*) $|\Delta \boldsymbol{X}|/d_I \leqslant 0.25$, (*c*) $|w|\Delta t/\Delta z_0 < 0.25$, (*d*) $M|\Delta \boldsymbol{u}|\Delta t/d_I < 0.05$, (*e*) $1.2 < D_0 < 1.5$. While these optimal criteria are a good general combination, modified values can be used for particular flow fields by reference to the appropriate figures.

In order to achieve these optimal parameters the following PIV experimental design procedure can be adopted. To maintain spatial resolution and restrict

effects of out-of-plane motion, choose d_I and Δz_0, based on *a priori* knowledge of the flow field. The seeding density C should be determined such that $N_I \geqslant 15$, although this can be reduced if other parametric restrictions are small, so that $N_I \sim 10$–20. Then, choose Δt to minimize bias due to velocity gradients, minimize pair losses due to out-of-plane motion and give adequate image displacements as in criteria (b), (c) and (d) above.

The above recommendations and conclusions pertain to two pulse, planar PIV with analysis by full 2-D spatial correlation or equivalently by 2-D Fourier transform of Young's fringes. Analysis of a multipulse system with three or more pulses is continuing and will be considered separately.

Acknowledgment

This material is based on work supported by the National Science Foundation under Grant Nos ATM 86–00509 and ATM 90–20605.

References

Adrian R J 1984 Scattering particle characteristics and their effect on pulsed laser measurements of fluid flow: speckle velocimetry vs. particle image velocimetry *Applied Optics* **23** 1690

—— 1985 Multi-point vector measurement by pulsed laser velocimetry with image compression *Proc. Int. Symp. on Fluid Control and Measurement* (Oxford: Pergamon) p 1087

—— 1986 Multipoint optical measurements of simultaneous vectors in unsteady flow—a review *Int. J. Heat and Fluid Flow* **7** 127

—— 1988a Statistical properties of particle image velocimetry measurements in turbulent flow *Laser Anemometry in Fluid Mechanics* Vol. III (LADOAN Institute Superior Tecnico, Lisbon, Portugal) 115

—— 1988b Double exposure, multiple field particle image velocimetry for turbulent probability density *Opt. Lasers Eng.* **9** 211

Adrian R J and Yao C S 1983 Development of pulsed laser velocimetry for measurement of fluid flow *Proc. 8th Symp. on Turbulence* (*University of Missouri Rolla*) p 170

Barker D B and Fourney M E 1977 Measuring fluid velocities with speckle patterns *Opt. Lett.* **1** 135

Burch J M and Tokarski J M J 1968 Production of multiple beam fringes from photographic scatters *Opt. Acta* **15** 101

Dudderar T D, Meynart R and Simpkins P G 1988 Full field laser metrology for fluid velocity measurement *Opt. Lasers Eng.* **9** 163

Grousson R and Malleck S 1977 Study of flow pattern in a fluid by scattered laser light *Appl. Opt.* **16** 2334

Hesselink L 1988 Digital image processing in flow visualization *Ann. Rev. Fluid Mech.* **20** 421

Landreth C C and Adrian R J 1989 Measurement and refinement of velocity data using high image density analysis in particle image velocimetry *Applications of Laser Anemometry to Fluid Mechanics* ed R J Adrian *et al* (Berlin: Springer) p 484

Landreth C C, Adrian R J and Yao C S 1988 Double pulsed particle image velocimeter with directional resolution for complex flows *Exp. Fluids* **6** 119

Lauterborn W and Vogel A 1984 Modern optical techniques in fluid mechanics *Ann. Rev. Fluid Mech.* **16** 223

Lourenco L and Krothapalli A 1987 The role of photographic parameters in laser speckle or particle image displacement velocimetry *Exp. Fluids* **5** 29

Meynart R 1983 Instantaneous velocity field measurements in unsteady gas flow by speckle velocimetry *Appl. Opt.* **22** 535

Reuss D L, Adrian R J, Landreth C C, French D T and Fansler T D 1989 Instantaneous planar measurements of velocity and large-scale vorticity and strain rate in an engine using particle image velocimetry *Society of Automotive Engineers paper 890616*

Simpkins P G and Dudderar T D 1978 Laser speckle measurement of transient Bénard convection *J. Fluid Mech.* **89** 665

Yao C S and Adrian R J 1984 Orthogonal compression and 1-D analysis technique for measurement of particle displacements in pulsed laser velocimetry *Appl. Opt.* **23** 1687